Capillarity

Vol. 18, No. 3, p. 96-105, 2026

Original article

Micro-CT-based pore-network analysis of carbonate rock dissolution: Linking microstructural evolution to permeability enhancement

Darezhat A. Bolysbek[1]*, Alibek B. Kuljabekov[1]*, Kenbai Sh. Uzbekaliyev[1], Bakytzhan K. Assilbekov[2]

[1]*Institute of Ionosphere, 117 "Ionosphere", Almaty 050020, Kazakhstan*
[2]*M. Auezov South Kazakhstan University, Shymkent 160012, Kazakhstan*

Keywords:
Carbonate dissolution
micro-CT imaging
pore-network modeling
permeability evolution
reactive flow

Cited as:
Bolysbek, D. A., Kuljabekov, A. B., Uzbekaliyev, K. Sh., Assilbekov, B. K. Micro-CT-based pore-network analysis of carbonate rock dissolution: Linking microstructural evolution to permeability enhancement. Capillarity, 2026, 18(3): 96-105.
https://doi.org/10.46690/capi.2026.03.02

Abstract:
Understanding how carbonate rock microstructure evolves during dissolution is essential for optimizing acid stimulation and assessing the integrity of carbon dioxide storage reservoirs. In this study, four carbonate core samples subjected to hydrochloric acid flooding were analyzed using micro-computed tomography and pore-network modeling to quantify changes in pore geometry and transport properties. Three-dimensional digital reconstructions of pre- and post-dissolution volumes revealed significant restructuring of the pore system, including the coalescence of small pores and the formation of new flow channels. Quantitative analysis showed that the mean pore and throat radii increased substantially, accompanied by a marked rise in connected porosity. These morphological changes led to a substantial enhancement in absolute permeability, while hydraulic tortuosity generally decreased. The extent of microstructural restructuring varied markedly among the analyzed sub-samples, reflecting differences in their initial pore architecture and dissolution patterns. Changes in pore-network topology and throat connectivity exerted a stronger control on permeability than uniform pore-size enlargement alone. Higher injection rates promoted the formation of localized preferential flow pathways by enhancing advective transport, which strongly influenced the resulting permeability evolution. The results highlight the critical role of dissolution heterogeneity and injection rate in controlling permeability evolution, providing pore-scale insights. The results provide pore-scale insights primarily applicable to carbonate acidizing processes, while also offering qualitative implications for carbon dioxide-brine – carbonate systems.

1. Introduction

Studying how mineral dissolution alters the microstructure of porous media is crucial for both enhancing hydrocarbon recovery from carbonate reservoirs and for long-term CO_2 storage in aquifers. For example, Vafaie et al. (2023) showed that injecting CO_2-saturated brine (a weak carbonic acid) into limestone can induce wormholes that drastically increase permeability while weakening the rock's mechanical integrity. Khojastehmehr et al. (2025) similarly emphasize that CO_2 produced during acid-carbonate reactions can significantly affect wormhole propagation through multiple mechanisms (e.g., changes in relative permeability, surface area and dif-

Yandy Scientific Press

*Corresponding author.
E-mail address: bolysbek.darezhat@gmail.com (D. A. Bolysbek); alibek.kuljabekov@gmail.com (A. B. Kuljabekov); kzkenbai@gmail.com (K. Sh. Uzbekaliyev); assilbekov.b@gmail.com (B. K. Assilbekov).

Received December 15, 2025; revised January 16, 2026; accepted February 2, 2026; available online February 5, 2026.

fusivity). Carbonate formations are predominantly composed of calcite and dolomite, which are commonly dissolved using hydrochloric acid solutions. During CO_2 injection, dissolution of the carbonate matrix occurs in addition to CO_2 dissolving in water, affecting porosity and permeability evolution.

Pore-scale dissolution of rocks is governed by numerous coupled physical and chemical processes that control microstructure evolution and the associated porosity-permeability relationship. These modifications depend on rock heterogeneity and dissolution conditions such as injection rate and fluid composition (Golfier et al., 2002; Luquot and Gouze, 2009; Molins et al., 2014; Agrawal et al., 2020). Previous studies have investigated factors controlling wormhole formation and dissolution patterns in carbonate rocks. Kalia and Balakotaiah (2007, 2009) demonstrated that at low acid-injection rates, the size of the investigation domain strongly influences dissolution efficiency, while at high injection rates, this effect becomes negligible. Cohen et al. (2008) further highlighted that sample geometry can substantially disrupt wormholing by suppressing the competition mechanism among developing wormholes. Ghommem et al. (2015) used a two-scale numerical model to show that at optimal injection rates, wormhole width remains nearly constant along the sample length, whereas conical wormholes exhibit a linearly decreasing width. More recent investigations have further refined these models to account for the mineral dissolution and wormhole formation at the pore-scale (Soulaine et al., 2021). Mota (2024) provides a comprehensive review of carbonate acidizing, highlighting that acid concentration, injection rate, and rock heterogeneity are the key factors shaping wormhole geometry. Zhang et al. (2024) developed a detailed pore-scale model of acid-rock reaction and identified five distinct dissolution modes in carbonates – uniform dissolution, compact dissolution, conical wormholes, dominant wormholes, and ramified wormholes – under different flow and chemistry conditions. Furui and Yoshioka (2025) showed using a phase-field approach that wormholes can form even in macroscopically homogeneous media (given a suitable inlet velocity), and that increasing heterogeneity can actually suppress wormhole growth and lower overall injectivity. Recent low-flow experiments by Neyra et al. (2025) indicate that traditional models tend to overestimate the pore volume to breakthrough at very low injection rates, meaning actual wormhole breakthrough can occur earlier than predicted under highly reactive conditions. In one of the latest pore-scale studies, Wang et al. (2026) simulated CO_2-brine reactive flow in a natural carbonate sample and observed three dissolution regimes: Uniform, conical wormhole, and ramified wormhole. They found that a higher fraction of reactive mineral content drives the system toward the conical wormhole mode, which markedly enhances CO_2 injectivity and storage capacity. These findings reinforce that both mineralogical and structural heterogeneity critically influence how dissolution proceeds and how permeability is enhanced.

One effective approach for understanding the complexity of rock dissolution is the use of pore-scale models, particularly pore-network and lattice-Boltzmann models. Numerous pore-network models have been developed to represent the topology of porous media and the geometry of individual pores (e.g., Al-Gharbi and Blunt, 2005; Raoof et al., 2013). In the context of rock dissolution, these models often employ networks of spherical pores connected by cylindrical throats to simulate reactive flow (Raoof and Hassanizadeh, 2012; Menke et al., 2015). Such models provide porosity-permeability relations that depend on dissolution conditions, which is essential for upscaling to larger scales. These approaches form the foundation for linking pore-scale processes to macroscopic flow behavior. More recently, machine-learning techniques have been incorporated to bridge the pore and continuum scales. For instance, Alzahrani et al. (2023) introduced a "Pore-GNN" framework that uses a graph neural network (GNN) on three-dimensional micro-CT pore-space images to predict absolute permeability directly from pore-scale features. Emeliana et al. (2026) systematically review the coupling of lattice-Boltzmann simulations with deep learning, noting that machine learning (convolutional neural network/GNN) can greatly accelerate predictions of porosity and permeability from digital rock images while lattice boltzmann method captures detailed flow physics. These AI-assisted models complement classical pore-network methods by efficiently handling large, heterogeneous datasets.

In recent years, pore-scale characterization and modeling of fluid transport in carbonate and other complex reservoirs have advanced significantly, driven by developments in digital rock physics and multiscale methods. Recent studies have focused on constructing realistic digital carbonate models from micro-CT data, coupling pore-network or lattice boltzmann method models with direct numerical simulations, and investigating micro- and nano-scale flow mechanisms (Zhao et al., 2023; Qin et al., 2024; Song et al., 2024). For example, Kashani et al. (2024) used lattice-Boltzmann simulations to compare dissolution in single-porosity versus dual-porosity carbonates, and found that wormholes in dual-porosity media tend to be narrower and more elongated than those in single-porosity media (due to altered reactive surface distribution). Such studies emphasize that the details of pore geometry, throat-size distribution, and network connectivity play a dominant role in controlling permeability and flow efficiency in heterogeneous carbonates.

However, despite these advances, quantitative pore-scale analyses based on real carbonate cores imaged before and after chemical dissolution remain relatively scarce, particularly for linking microstructural evolution directly to permeability enhancement under different reactive flow conditions. The present study addresses this gap by performing a quantitative pore-scale analysis of actual carbonate rock samples subjected to hydrochloric acid flooding, combining high-resolution micro-computed tomography with pore-network modeling. Unlike many previous studies relying on synthetic or numerically dissolved pore structures, this work directly compares identical sub-volumes of carbonate cores before and after dissolution, enabling a consistent assessment of microstructural evolution. Changes in pore and throat size distributions, coordination number, connected porosity, hydraulic tortuosity, and absolute permeability are systematically analyzed for different acid concentrations and injection rates. The results provide new insights into the role of dissolution

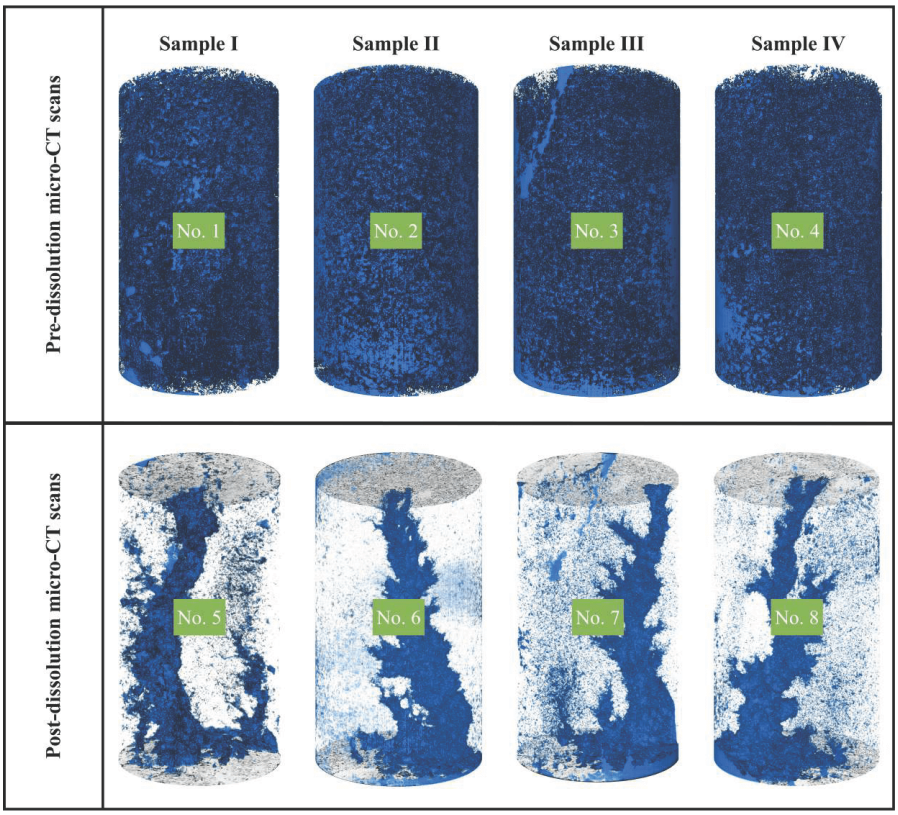

Fig. 1. Selected mini-samples and cylindrical cores.

heterogeneity and flow conditions in controlling permeability enhancement, with direct relevance to practical reservoir engineering applications such as carbonate acidizing and CO_2 injection in geological formations.

2. Materials and methods

2.1 Materials

The dataset comprised four cylindrical carbonate cores, each ~5 cm in length and ~3 cm in diameter, which were subjected in the laboratory to core-flood experiments with hydrochloric-acid-based solutions and subsequently scanned using a micro-computed tomography system with a spatial resolution of ~19 μm. Cores I and II were injected with 18% and 12% HCl, respectively, at a flow rate of 8 mL/min, whereas Cores III and IV received the same acid concentrations at a lower flow rate of 4 mL/min. The acid concentrations (12 and 18 wt% HCl) and injection rates (4 and 8 mL/min) were selected to form a simple 2×2 design that spans two practically relevant levels of chemical reactivity and advective transport intensity. This matrix is intended to qualitatively probe changes in dominant dissolution regimes (more uniform versus more localized channeling/wormholing) and to isolate first-order effects of (i) acid strength at fixed flow rate and (ii) flow rate at fixed acid strength, while keeping the experimental campaign feasible for micro-CT imaging and pore-network extraction.

The injection rates and hydrochloric acid concentrations were selected to represent distinct dissolution regimes commonly discussed in carbonate acidizing studies. Specifically, lower injection rates combined with higher acid concentrations were intended to promote more localized dissolution, while higher injection rates at lower acid concentrations favor more distributed reaction fronts. This experimental design allows the influence of flow conditions and chemical strength on pore-scale dissolution patterns to be examined in a comparative manner, while remaining within ranges relevant to practical carbonate reservoir stimulation.

The tomographic images were processed, and three-dimensional digital models of Cores I-IV were reconstructed by volume rendering in Avizo. Prior to pore-network extraction, the micro-CT images were preprocessed using a median filter with a smoothing radius of 3 voxels to reduce high-frequency noise. Pore space segmentation was performed in Avizo using an interactive global thresholding procedure followed by a watershed-based separation to refine pore and throat boundaries. The watershed segmentation employed a marker extent parameter of 1, selected to achieve stable separation of connected pore regions without over-segmentation. All segmentation and pore-network extraction parameters were kept identical for all pre- and post-dissolution datasets to ensure consistency and reproducibility.

To investigate the changes in pore structure induced by acid injection, digital models of the carbonate cores were analyzed before and after dissolution. The top and bottom panels of Fig. 1 show the pre- and post-dissolution states, respectively, with dark-blue regions in the bottom panels highlighting flow channels (wormholes) formed by dissolution. For quantitative

analyses, eight cubic sub-samples (Nos. 1-8) with side lengths of approximately 7 mm were extracted from these cores, as indicated in green in Fig. 1. The choice of smaller sub-samples reflects constraints on computational resources and simulation time. Accordingly, from the pre- and post-dissolution volumes of each cylindrical core, one cubic sub-sample was cut, yielding a total of eight sub-volumes: Four "before" and four "after". Each post-acid sub-sample was taken from the same spatial location as its pre-acid counterpart and preserved identical dimensions. Due to the high computational cost associated with pore-network extraction and flow simulation on high-resolution micro-CT data, the analysis was limited to one cubic sub-sample per core for the pre- and post-dissolution states. The selected sub-samples were extracted away from the outer boundaries of the cylindrical cores and inlet/outlet faces to minimize edge effects. While this approach does not fully capture the spatial heterogeneity of the entire core, it enables a consistent pore-scale comparison of dissolution-induced structural changes under different flow rates and acid concentrations. The implications of this limitation are discussed further in the Conclusions.

2.2 Methods

Changes in the pore structure of the sub-samples were investigated using pore-network modeling of fluid flow in porous media. In this approach, a pore network is first constructed from the segmented pore space of the real rock sample. Network extraction from the segmented images was performed with Avizo software (TFS, 2019). The resulting network consists of spheres (idealized pores) and cylinders (idealized pore throats) with varying radii. After building the network, single-phase flow is simulated on it: Phase pressures are computed at pore centers from mass conservation, and fluid velocities are determined within the cylindrical throats. From the resulting pressure and velocity fields, macroscopic parameters, such as absolute permeability and hydraulic tortuosity are subsequently evaluated. The segmented pore space was first divided into individual particles, which were subsequently treated as distinct pores. The next step involved generating markers at the centers of these particles. The marker generation followed the following algorithm:

1) computation of a distance map for each particle;
2) extraction of the particle skeleton;
3) masking of the distance map using the skeleton;
4) identification and labeling of particle (grain) centers on the masked distance map.

In this workflow, pore bodies are identified based on the maximum inscribed sphere concept, where each pore is represented by a sphere whose radius corresponds to the local maximum of the distance map within the segmented pore space. The distance transform assigns to each voxel the minimum distance to the solid-pore interface, and local maxima of this field are used to define pore centers and equivalent pore radii. Connectivity between neighboring pores is determined along the medial axis (skeleton) of the pore space, which represents the central pathways of the void geometry.

Pore throats are subsequently defined along the skeleton as constrictions between adjacent pores. Each throat is approximated as a cylindrical element whose radius corresponds to the minimum distance to the solid phase along the connecting path, while the throat length is defined as the distance between the centers of the connected pores. This marker-based watershed and skeletonization approach allows the complex pore geometry extracted from micro-CT images to be reduced to a simplified pore-network representation composed of spherical pores and cylindrical throats, while preserving the essential topological and geometric characteristics of the real porous medium.

An important factor in this process is the selection of the contrast coefficient, as higher values lead to an increased number of merged particles. Consequently, this image-processing stage is highly sensitive to the operator's adjustments and experience (Li et al., 2021). After isolating the pore space into separate regions, a corresponding pore-network model can be generated in which pores are represented as spheres and throats as cylinders. The extracted network provides the following statistics: Number of pores, number of throats, coordination number, equivalent throat radius and throat length (defined as the distance from a pore to the center of the next connected pore), fluid velocity in each throat, pore volume, and equivalent pore radius. Each sphere and cylinder can be color-mapped according to its radius. Pore size and color are thus expressed via the equivalent pore radius, and throat size and color via the throat (channel) length.

From the pore network, one can derive parameters such as the pore and throat size distributions, porosity, specific pore surface area, and coordination number, as well as compute tortuosity and absolute permeability. To evaluate absolute permeability, the network is assumed to be fully saturated with a single phase. For steady, incompressible flow, mass conservation for each pore body is written as (Darcy, 1856; Fatt, 1956):

$$\Sigma g_{ij}(P_i - P_j) = 0 \tag{1}$$

where the summation is performed over all pores j, connected to pore i, P_i and P_j are the pressures at the centers of pores i, j, respectively. Since the pore throats are represented as cylindrical tubes with radius r_{ij} and length l_{ij}, their hydraulic conductance g_{ij} is determined according to Poiseuille's law:

$$g_{ij} = \frac{\pi r_{ij}^4}{8\mu l_{ij}} \tag{2}$$

where μ is the dynamic viscosity of the fluid.

The absolute permeability k of the sub-sample is calculated according to Darcy's law:

$$k = \frac{Q\mu L}{\Delta P A} \tag{3}$$

where ΔP is the pressure drop applied across the ends of the sub-sample, L is the length of the sub-sample along the flow direction, Q is the total volumetric flow rate through the medium, and A is the cross-sectional area of the sub-sample perpendicular to the flow direction.

The hydraulic tortuosity is calculated based on the fluid

Table 1. Langmuir model and empirical equations for monolayer sorption.

No.	r_p (μm)	r_t (μm)	ϕ (%)	S (μm^{-1})	n_e (-)	τ (-)	k (-)
1	117.0	53.4	16.4	22.5	5.7	1.57	4.3
2	100.0	45.4	14.0	32.6	2.9	1.92	0.8
3	89.8	38.6	8.7	40.2	2.6	1.87	0.002
4	90.7	39.4	12.2	36.6	2.7	1.94	0.03

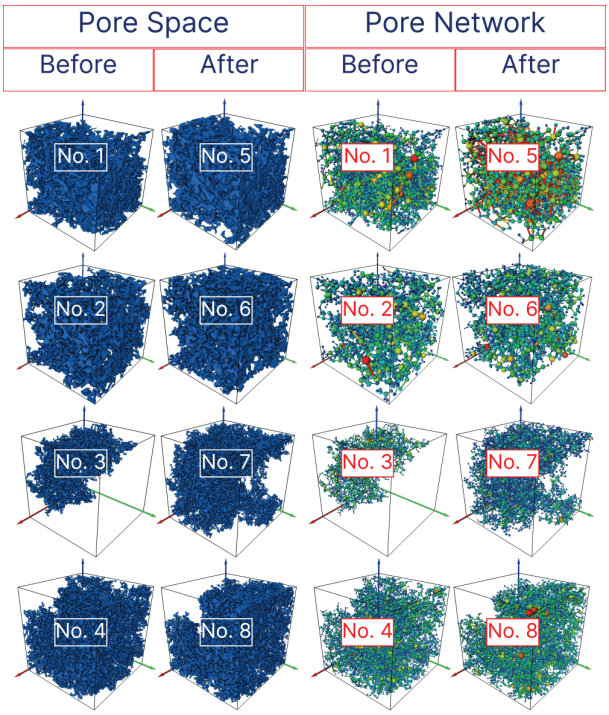

Fig. 2. Segmented pore space and corresponding pore-network models before and after dissolution.

velocities obtained during the permeability estimation. Knowing the velocity in each pore throat, the tortuosity τ is determined as the ratio of the sum of all velocity magnitudes to the sum of their projections along the main flow direction (Bear, 1972):

$$\tau = \frac{\sum_{i=1}^{n} ||v_i||}{\sum_{i=0}^{n} ||v_{xi}||} \tag{4}$$

where n is the number of throats, v_i is the fluid velocity through throat i, and v_{xi} is its projection onto the axis parallel to the main flow direction.

3. Results and discussion

3.1 Pore space and pore network

The segmented pore spaces (first two columns) and the corresponding pore-network models constructed from them (last two columns) before and after rock dissolution are shown in Fig. 2. In this study, two-phase segmentation was performed, that is, separation of the pore space from the solid skeleton, since the samples were thoroughly washed and dried prior to scanning. Note that only the pore spaces belonging to connected pores and their corresponding pore networks are displayed. The pore space is rendered in dark blue, while the pore network is color-mapped to show all pores and throats according to their sizes. In all pore-network visualizations, the same color-size mapping is applied to both pre- and post-dissolution states to enable direct visual comparison. Warmer colors correspond to larger equivalent pore or throat radii, whereas cooler colors indicate smaller pore and throat sizes.

To compare the pore structure across the four sub-samples, the sizes and connectivity of pores and throats were analyzed. Sub-samples No. 1 and No. 2 were found to contain larger pores compared with sub-samples No. 3 and No. 4. On average, the mean pore radius and mean throat radius in sub-samples No. 1 and No. 2 are approximately 20% and 25% higher, respectively, than those in sub-samples No. 3 and No. 4 (Table 1). Fig. 2 illustrates these differences visually. Table 1 reports the mean values of key parameters prior to dissolution: Mean pore radius (r_p), mean throat radius (r_t), connected porosity (ϕ), mean specific pore surface area (S), mean coordination number (n_c), mean tortuosity (τ), and mean permeability (k). Another distinction between sub-samples No. 1-2 and No. 3-4 is that the former exhibit higher inter-pore connectivity, as reflected by their larger coordination numbers.

To clarify the controlling factors, this study compared paired cases that differ by a single variable. At fixed flow rate (8 mL/min), increasing acid concentration from 12 to 18 wt% (Core II, Core I) primarily increases the extent of pore enlargement and connectivity gain, reflected by larger mean pore and throat radii and higher connected porosity. At fixed acid concentration, increasing flow rate from 4 to 8 mL/min (Core III, Core I for 18 wt% and Core IV, Core II for 12 wt%) promotes more localized channel development and stronger permeability gains, consistent with advectively driven reactive infiltration instability (wormholing). Therefore, within the tested parameter space, permeability enhancement is governed by the coupled effect of transport and reaction: Flow rate controls the degree of channel localization, while acid concentration controls the available reaction capacity. Therefore, within the tested parameter space, permeability enhancement is governed by the coupled effect of transport and reaction: Flow rate controls the degree of channel localization, while acid concentration controls the available reaction capacity. From a reactive transport perspective, the observed transition between uniform and localized dissolution regimes can be qualitatively interpreted in terms of the balance between advection and reaction rates, commonly described by the Péclet and Damköhler numbers (Szymczak and Ladd, 2009; Egermann et al., 2010; Roded et al., 2020; Menke et al., 2023), although a quantitative evaluation of these dimensionless parameters is beyond the scope of the present study.

The strongest permeability increase (sub-sample No. 3) is interpreted as a case where dissolution created a continuous preferential pathway connecting inlet to outlet, whereas minimal change (sub-sample No. 2) indicates either more

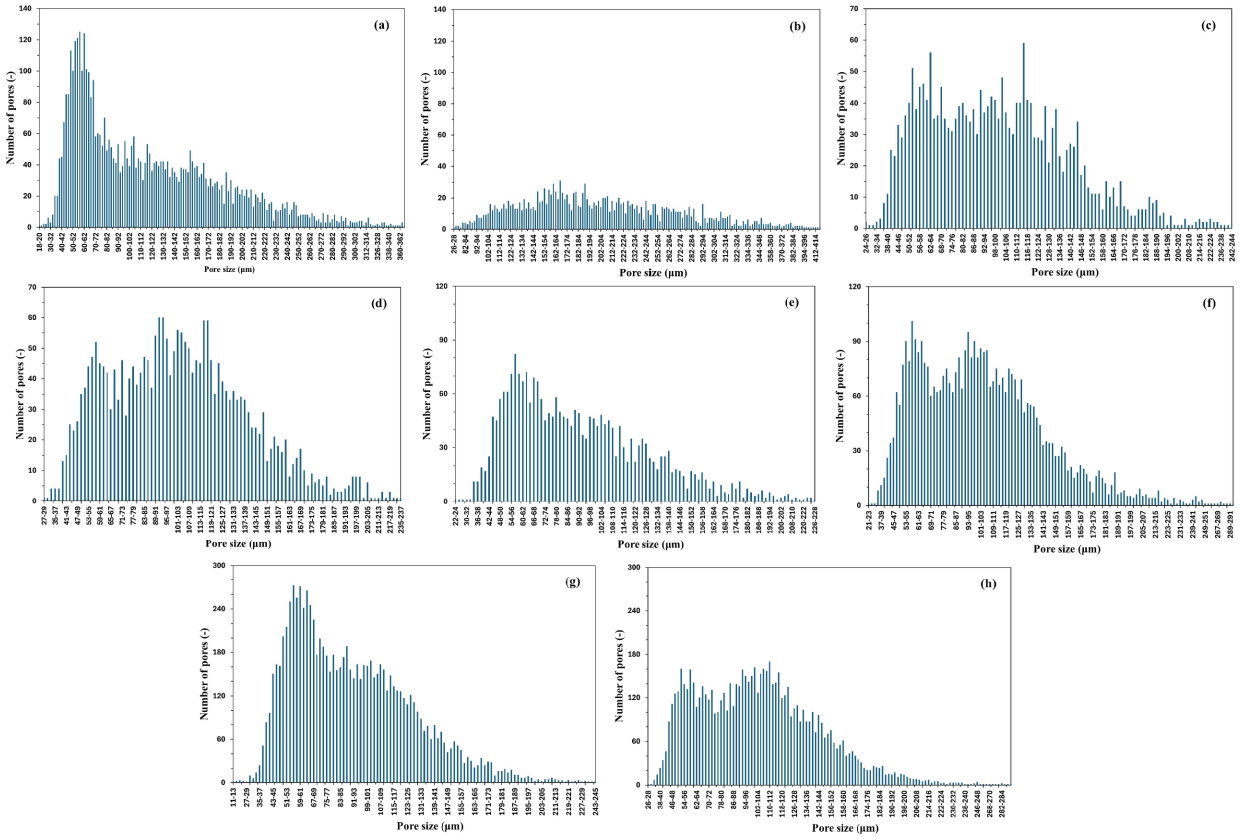

Fig. 3. Pore-size distributions of sub-samples Nos. 1-4 before and after dissolution: (a) No. 1, (b) No. 5, (c) No. 2, (d) No. 6, (e) No. 3, (f) No. 7, (g) No. 4 and (h) No. 8.

uniform dissolution without establishing a spanning channel or dissolution constrained to zones that do not significantly contribute to through-flow.The strongest permeability increase (sub-sample No. 3) is interpreted as a case where dissolution created a continuous preferential pathway connecting inlet to outlet, whereas minimal change (sub-sample No. 2) indicates either more uniform dissolution without establishing a spanning channel or dissolution constrained to zones that do not significantly contribute to through-flow. Overall, multiple parameters vary among the four sub-samples, the observed trends allow qualitative insights into the dominant controlling factors of permeability enhancement.

3.2 Pore size distribution

One key descriptor of the pore structure is the distribution of pore and throat sizes. Fig. 3 shows pore-size distributions for sub-samples Nos. 1-4 before and after dissolution. The pore-size distributions shown in Fig. 3 are derived from the pore-network representation of the segmented micro-CT images. Each pore body is represented as a spherical element obtained using the maximum inscribed sphere approach, and the pore size is quantified by the equivalent pore radius corresponding to the local maximum of the distance map within the pore space. As a result, the pore-size distribution primarily reflects the volumetric characteristics of the pore bodies and their contribution to fluid storage within the porous medium.

In sub-sample No. 1, pores with radii of 56-58 μm dominated prior to dissolution (Fig. 3(a)), although the mean pore radius over the whole sample was 117 μm (see Table 2). After injecting 18% HCl at 8 mL/min, the distribution shifted markedly, with pores of approximately 170 μm becoming predominant (Fig. 3(b)). The mean pore radius increased to 203 μm, a rise of 74%. In addition, the range of connected pore radii broadened from 18-368 μm to 26-422 μm, indicating that the smallest pores with radii of 18-20 μm disappeared, either merging into larger pores or expanding due to dissolution. A substantial reduction in the fraction of relatively small pores is also evident.

In sub-sample No. 2, the pre-dissolution pore sizes exhibit a bimodal distribution, i.e., two dominant size intervals. Before injecting 12% HCl at 8 mL/min, most pores fell within 50-64 μm and 110-124 μm (Fig. 3(c)). After dissolution, the fraction of pores with radii 89-127 μm increased substantially, although the mean pore radius for the entire sub-sample grew by only ∼3% (see Table 2). Moreover, the distribution became smoother, indicating reduced size heterogeneity following acid injection, while the bimodal character was retained (Fig. 3(d)).

Because the original histogram binning and raw distribution data were not retained, the pore- and throat-size distributions are compared using consistent relative ranges within each sub-sample, while all quantitative interpretations are based on the statistical metrics reported in Tables 1 and 2. In sub-samples Nos. 3 and 4, the initially bimodal pore-

Table 2. Comparative metrics before vs. after dissolution.

Sub-sample		r_p (μm)	r_t (μm)	ϕ (%)	S (μm^{-1})	n_e	τ	k (μm^2)
1	Before	117.0	53.4	16.4	22.5	5.7	1.57	4.3
	After	203.3	73.0	20.3	19.1	6.2	1.40	11.0
2	Before	100.0	45.4	14.0	32.6	2.9	1.92	0.8
	After	103.0	44.4	16.0	30.4	3.0	1.86	1.0
3	Before	89.8	38.6	8.7	40.2	2.6	1.87	0.002
	After	98.6	42.6	11.7	32.7	2.7	1.97	0.13
4	Before	90.7	39.4	12.2	36.6	2.7	1.94	0.03
	After	103.3	45.6	13.2	31.3	2.96	1.91	0.17

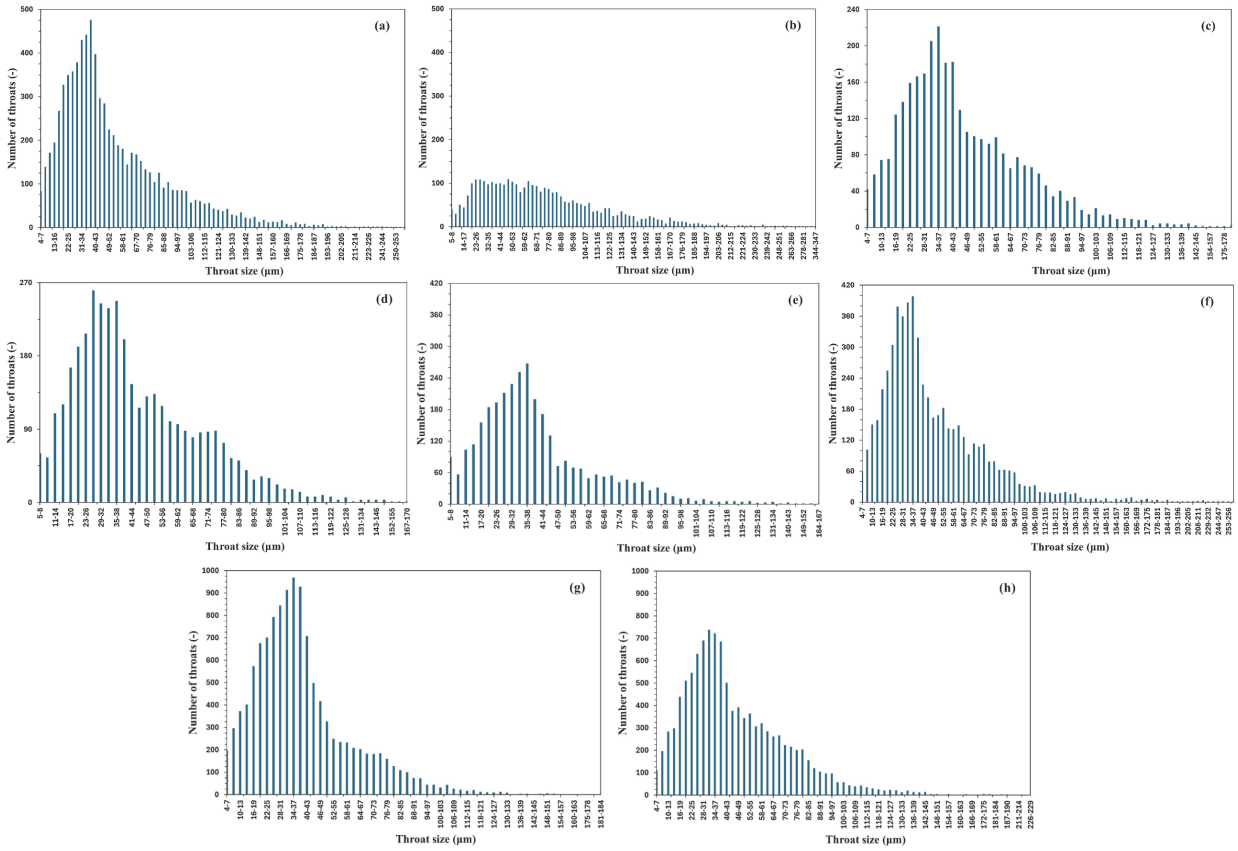

Fig. 4. Pore-throat size distributions of sub-samples Nos. 1-4 before and after dissolution: (a) No. 1, (b) No. 5, (c) No. 2, (d) No. 6, (e) No. 3, (f) No. 7, (g) No. 4 and (h) No. 8.

size distributions persisted after dissolution, but the ranges of pore radii changed. Most notably, the upper bounds of these ranges increased by ∼20% in both cases (Fig. 3(e) and 3(g)). In sub-sample No. 3, new pores with radii around 21 μm appeared after dissolution; conversely, in sub-sample No. 4 the lower bound shifted from 11-13 μm to 26-28 μm, indicating substantial coarsening of the smallest pores. Additionally, in both sub-samples the population of pores near the mean radius (see Table 2), which effectively forms secondary peaks within the bimodal distribution, increased markedly following injection of 18% HCl (No. 3) and 12% HCl (No. 4) at 4 mL/min. The mean pore radius in both cases rose by approximately 10%. Overall, the total number of pores increased by roughly 1.5× after dissolution in both sub-samples, as also evident in Fig. 2 (sub-samples Nos. 7 and 8).

3.3 Pore-throat size distribution

The pore-throat size distributions presented in Fig. 4 are based on the radii of the connecting throats between adjacent pore bodies in the pore-network model. Throats are identified along the medial axis of the pore space as constrictions

between neighboring pores, and their sizes are quantified by the minimum distance to the solid phase along the connecting pathway. Therefore, the throat-size distribution characterizes the narrowest flow passages in the pore network, which play a dominant role in controlling hydraulic conductance and permeability.

For sub-sample No. 1, the throat-size distribution changed markedly (Fig. 4(a)). A previously narrow peak broadened substantially after dissolution (Fig. 4(b)), indicating that a portion of the throats became larger, thereby forming micro-channels for fluid flow. In addition, both the lower and upper bounds of the throat-radius range shifted to larger values, consistent with pervasive dissolution. Because increasing throat diameter enhances volumetric flux, these changes strongly affect the sample's absolute permeability. As shown in Table 2, a 37% increase in the mean throat radius of sub-sample No. 1 led to a 2.5× increase in absolute permeability. A similar trend is observed for sub-sample No. 4 (Figs. 4(g) and 4(h)).

For sub-samples Nos. 2 and 3, the number of throats increased after dissolution (Figs. 4(c) and 4(e)). The effect is especially pronounced in sub-sample No. 3, where the throat-radius range widened considerably, signaling the formation of new connections between previously disconnected pores. This created new flow pathways, boosting the sample's transmission capacity; accordingly, the absolute permeability of sub-sample No. 3 increased by about 65× (Table 2).

The markedly different permeability responses observed between sub-samples No. 3 and No. 2 can be interpreted in terms of distinct dissolution regimes. In sub-sample No. 3, the combination of initial pore-network connectivity and flow conditions favored localized, channelized dissolution, leading to the formation of preferential flow pathways that significantly reduced hydraulic resistance. Once a continuous high-conductivity channel was established, permeability increased disproportionately relative to the overall pore-size enlargement. In contrast, sub-sample No. 2 exhibited a more uniform dissolution regime, characterized by distributed pore and throat enlargement without the development of dominant flow channels, resulting in comparatively modest permeability changes despite measurable increases in pore size.

The exceptionally large permeability increase observed for sub-sample No. 3 is attributed to the formation of a continuous preferential flow pathway spanning the inlet and outlet of the analyzed volume. Microstructural inspection of the pore-network maps (Fig. 2) indicates pronounced enlargement and coalescence of pores along a dominant dissolution channel, accompanied by the creation of new pore-throat connections. This process markedly reduces hydraulic resistance by increasing both throat radii and network connectivity, resulting in a non-linear amplification of permeability that far exceeds the corresponding increase in porosity.

These observations further support the qualitative sensitivity assessment, suggesting that sub-samples subjected to higher effective reactant fluxes exhibit more pronounced permeability enhancement due to the formation of preferential flow pathways. In sub-sample No. 2, throats with the largest radii disappeared (Figs. 4(b) and 4(c)), likely because these throats converted into pores as dissolution progressed. This transformation is consistent with a more homogeneous dissolution regime, in which existing wide conduits are progressively smoothed into pore bodies rather than reorganized into a preferential through-going flow channel.

To quantify how dissolution alters pore-network connectivity and void space, the key structural parameters of all sub-samples before and after dissolution were compared. Table 2 presents the corresponding statistics. Notably, connected porosity increased by 8-34%. The largest porosity gain occurred in sub-sample No. 3, where numerous new inter-pore connections emerged, even though the mean coordination number rose by only about 4% after dissolution. This can be explained by the fact that, for this sub-sample, dissolution not only enhanced connectivity but also increased the total number of pores (see Fig. 2, sub-sample No. 7). The greatest increase in coordination number, approximately 9%, was observed in sub-sample No. 1. A decrease in tortuosity was recorded for all sub-samples except No. 3. Tortuosity characterizes the average path length of fluid particles along the flow direction: The greater the medium's resistance, the higher the tortuosity and, consequently, the lower the absolute permeability. The slight increase in tortuosity observed for sub-sample No. 3 can be attributed to the highly localized nature of dissolution in this case. While permeability increased dramatically due to the formation of a dominant preferential flow pathway, the remaining pore network outside this channel became relatively less connected and more convoluted. As a result, the global tortuosity metric, which reflects average transport pathways over the entire pore network, may increase despite the presence of a highly conductive channel. This observation highlights that tortuosity and permeability do not necessarily evolve monotonically and can respond differently to strongly heterogeneous dissolution patterns.

It should be noted that the dissolution patterns and permeability responses observed in this study are specific to strong-acid (HCl) injection, which is characterized by rapid reaction kinetics and high local dissolution rates. In contrast, carbonate dissolution driven by carbonic acid, relevant to CO_2 injection and geological carbon storage, typically proceeds under weaker acidity and slower reaction rates, often resulting in more distributed and transport-limited dissolution regimes reported in the literature. Previous pore-scale and micro-CT studies have shown that carbonic acid dissolution tends to promote more gradual pore enlargement with less pronounced channel localization compared to hydrochloric acid. Therefore, while the pore-network-based insights obtained here are directly applicable to carbonate acidizing scenarios, their extension to CO_2-brine-carbonate systems should be interpreted with caution and requires dedicated investigation.

Although pore and throat enlargement during carbonate dissolution has been widely reported in previous experimental and numerical studies, the present work extends existing knowledge by quantitatively linking dissolution-induced microstructural evolution to permeability enhancement using a combined micro-CT and pore-network modeling framework applied to paired pre- and post-dissolution datasets. Unlike many prior studies that focus primarily on porosity changes or qualitative pore morphology, this study demonstrates how

localized changes in pore-network connectivity and throat topology can lead to highly non-linear permeability responses under different flow and chemical conditions. The comparative analysis across multiple dissolution scenarios highlights the dominant role of network reorganization, rather than uniform pore enlargement alone, in controlling permeability evolution.

4. Conclusions

The results demonstrate a pronounced impact of rock dissolution on pore structure as well as on the microscopic and macroscopic properties of the sub-samples. The most substantial restructuring of the pore space occurred in sub-sample No. 3. The largest changes is $\sim 74\%$ in mean pore radius, $\sim 37\%$ in mean throat radius, $\sim 34\%$ in connected porosity, and $\sim 19\%$ in the mean specific surface area of the solid matrix were observed in sub-samples Nos. 1, 3, and 4, leading to a significant increase in absolute permeability (2.5 times and 65 times). By contrast, sub-sample No. 2 exhibited only minor variations across most parameters and their distributions. The limited permeability enhancement observed for sub-sample No. 2 can be explained by differences in its initial pore structure and dissolution pattern.

In the sub-samples injected at a 4 mL/min acid flow rate, the number of pores increased for both larger and smaller radii classes. Overall, dissolution exerted a strong influence on the pore-size distribution. Across both acid concentrations and injection rates considered, the distributions became more distinctly bimodal following dissolution.

Based on the comparative analysis of the four dissolution conditions, several general influence trends can be identified. Increasing injection rate promotes the formation of localized preferential flow pathways by enhancing advective transport, which can lead to disproportionate permeability gains once a continuous channel is established. Higher acid concentration intensifies local dissolution and accelerates pore and throat enlargement, but does not necessarily result in significant permeability enhancement unless accompanied by favorable network connectivity. In all cases, changes in pore-network topology and throat connectivity exert a stronger control on permeability evolution than uniform pore-size growth alone, highlighting the dominant role of microstructural connectivity in carbonate dissolution processes.

Although the pore-network-derived permeability values were not directly validated against independent laboratory flow measurements for the same sub-samples, the obtained trends and orders of magnitude are consistent with experimental and numerical studies reported in the literature for carbonate dissolution under comparable conditions.

Several limitations of this study should be acknowledged. The pore-network analysis was conducted on a limited number of sub-samples extracted from each core, which may not fully capture the spatial heterogeneity of the original rock specimens. In addition, the dissolution experiments were performed using hydrochloric acid under laboratory-controlled conditions, and the resulting pore-scale responses may differ from those occurring during long-term carbonic acid dissolution associated with CO_2 injection. Future work should therefore focus on expanding the range of flow rates and reactant chemistries, incorporating repeated sub-sampling to improve statistical representativeness, and coupling pore-network modeling with reactive transport simulations to better link microstructural evolution with field-scale transport behavior.

Acknowledgements

This work was funded by the Committee of Science of the Ministry of Science and Higher Education of the Republic of Kazakhstan (No. AP23491018).

Conflicts of interest

The authors declare no competing interest.

References

Agrawal, P., Raoof, A., Iliev, T., et al. Evolution of pore-shape and its impact on pore conductivity during CO_2 injection in calcite: Single pore simulations and microfluidic experiments. Advances in Water Resources, 2020, 136: 103480.

Al-Gharbi, M. S., Blunt, M. J. Dynamic network modeling of two-phase drainage in porous media. Physical Review E, 2005, 71: 016308.

Alzahrani, M. K., Shapoval, A., Witthoeft, J., et al. Pore-GNN: A graph neural network-based framework for predicting flow properties of porous media from micro-CT images. Advances in Geo-Energy Research, 2023, 10: 39-55.

Bear, J. Dynamics of Fluids in Porous Media. American Elsevier Publishing Company, New York, USA, 1972.

Cohen, C. E., Ding, D., Quintard, M., et al. From pore scale to wellbore scale: Impact of geometry on wormhole growth in carbonate acidization. Chemical Engineering Science, 2008, 63(11): 3088-3099.

Darcy, H. The public fountains of the city of Dijon. Paris, France, Dalmont, 1856. (in French)

Egermann, P., Békri, S., Vizika, O., et al. An integrated approach to assess the petrophysical properties of rocks altered by rock-fluid interactions (CO_2 injection). Petrophysics - The SPWLA Journal of Formation Evaluation and Reservoir Description, 2010, 51: 11-20.

Emeliana, Y., Melkisedek, B. L., Arisbaya, I., et al. Integrating lattice Boltzmann and neural networks for modeling transport parameters in porous rocks: A systematic review. Results in Engineering, 2026, 29: 108688.

Fatt, I. The network model of porous media. Transactions of the American Institute of Mining, Metallurgical, and Petroleum Engineers, 1956, 207: 144-181.

Furui, K., Yoshioka, K. A phase-field modeling study for reaction instability and localized fluid flow in carbonate rocks. Geoenergy Science and Engineering, 2025, 245: 213438.

Ghommem, M., Zhao, W., Dyer, S., et al. Carbonate acidizing: Modeling, analysis, and characterization of wormhole

formation and propagation. Journal of Petroleum Science and Engineering, 2015, 131: 18-33.

Golfier, F., Zarcone, C., Bazin, B., et al. On the ability of a Darcy-scale model to capture wormhole formation during the dissolution of a porous medium. Journal of Fluid Mechanics, 2002, 457: 213-254.

Jiang, M., Xu, Z. G., Fan, L. C., et al. Pore-scale investigation on reactive flow in porous media considering dissolution and precipitation by LBM. Journal of Petroleum Science and Engineering, 2021, 204(2): 108712.

Kalia, N., Balakotaiah, V. Modeling and analysis of wormhole formation in reactive dissolution of carbonate rocks. Chemical Engineering Science, 2007, 62(4): 919-928.

Kalia, N., Balakotaiah, V. Effect of medium heterogeneities on reactive dissolution of carbonates. Chemical Engineering Science, 2009, 64(2): 376-390.

Kashani, E., Mohebbi, A., Monfared, A. E. F., et al. Lattice Boltzmann study of dissolution in porous media: Comparison of VOP with VOF-curved boundary coupling. Journal of Petroleum Science and Engineering, 2022, 216: 110754.

Khojastehmehr, M., Bazargan, M., Wood, D. A., et al. Reviewing CO_2 dynamics in acidizing carbonate reservoirs: Mechanisms, impacts, and models. Geoenergy Science and Engineering, 2025, 249: 213767.

Li, Y., Chi, Y., Wang, S., et al. Pore-throat structure characterization of carbon fiber reinforced resin matrix composites: Employing Micro-CT and Avizo technique. PLoS One, 2021, 16(10): e0257640.

Luquot, L., Gouze, P. Experimental determination of porosity and permeability changes induced by injection of CO_2 into carbonate rocks. Chemical Geology, 2009, 265: 148-159.

Menke, H. P., Bijeljic, B., Andrew, M. G., et al. Dynamic three-dimensional pore-scale imaging of reaction in a carbonate at reservoir conditions. Environmental Science and Technology, 2015, 49(7): 4407-4414.

Menke, H. P., Maes, J., Soulaine, C., et al. Channeling is a distinct class of dissolution in complex porous media. Scientific Reports, 2023, 13: 11312.

Molins, S., Trebotich, D., Steefel, C. I., et al. Pore-scale controls on calcite dissolution rates from flow-through laboratory and numerical experiments. Environmental Science and Technology, 2014, 48(13): 7453-7460.

Mota, T. M. Wormhole geometry modelling on carbonate matrix acidizing: A literature review. International Journal of Innovative Science and Research Technology, 2024, 9(6): 1345-1358.

Neyra, J. R., da Silva, D. N. N., Monteiro, A., et al. Carbonate acidizing: A new insight into wormhole propagation under low flow rates. ACS Omega, 2025, 10: 54086-54097.

Qin, X., Wang, H., Tang, H., et al. Micro- and nanoscale flow mechanisms in porous rocks based on pore-scale modeling. Capillarity, 2024, 13: 24-28.

Raoof, A., Hassanizadeh, S. M. A new formulation for pore-network modeling of two-phase flow. Water Resources Research, 2012, 48: W01529.

Raoof, A., Nick, H. M., Hassanizadeh, S. M., et al. PoreFlow: A complex pore-network model for simulation of reactive transport in variably saturated porous media. Computers and Geosciences, 2013, 61: 160-174.

Roded, R., Aharonov, E., Holtzman, R., et al. Reactive flow and homogenization in anisotropic media. Water Resources Research, 2020, 56(11): e2020WR027518.

Song, W., Liu, F., Meng, J., et al. Pore-scale modeling of fluid transport in complex reservoirs: Multi-scale digital rock construction, flow experiments and simulation methods. Capillarity, 2024, 11: 81-88.

Soulaine, C., Roman, S., Kovscek, A., et al. Mineral dissolution and wormhole formation in carbonate rocks at the pore-scale. Journal of Fluid Mechanics, 2021, 925: A32.

Szymczak, P., Ladd, A. J. C. Wormhole formation in dissolving fractures. Journal of Geophysical Research: Solid Earth, 2009, 114(B6): B06203.

Thermo Fisher Scientific (TFS). Avizo Software (version 2019.1). 1 March, 2019.

Vafaie, A., Cama, J., Soler, J. M., et al. Chemo-hydro-mechanical effects of CO_2 injection into a permeable limestone. International Journal of Coal Geology, 2023, 278: 104359.

Wang, J., Yang, Y., Wang, S., et al. Multi-mineral dissolution in 3D natural rock: Pore-scale reactive transport modeling for geological carbon storage. Chemical Engineering Science, 2026, 320: 122507.

Zhang, D., Li, Y., Wu, K., et al. Pore-Scale Numerical Simulation of Acid-Rock Reaction Processes in Carbonate Reservoirs. ACS Omega, 2024, 9(30): 34106-34117.

Zhao, J., Liu, Y., Zhang, W., et al. Pore-scale fluid flow simulation coupling lattice Boltzmann method and pore network model. Capillarity, 2023, 7: 41-46.